

Communication

Laser Additive Manufacturing of Oxide Dispersion-Strengthened Copper–Chromium–Niobium Alloys

Markus B. Wilms *  and Silja-Katharina Rittinghaus 

Chair of Materials Science and Additive Manufacturing, School of Mechanical Engineering and Safety Engineering, University of Wuppertal, Gausstr. 20, 42119 Wuppertal, Germany

* Correspondence: mwilms@uni-wuppertal.de; Tel.: +49-202-439-5392

Abstract: Copper is a key material for cooling of thermally stressed components in modern aerospace propulsion systems, due to its high thermal conductivity. The use of copper materials for such applications requires both high material strength and high stability at high temperatures, which can be achieved by the concept of oxide dispersion strengthening. In the present work, we demonstrate the oxide reinforcement of two highly conductive precipitation-strengthened Cu–Cr–Nb alloys using laser additive manufacturing. Gas-atomized Cu–3.3Cr–0.5Nb and Cu–3.3Cr–1.5Nb (wt.%) powder materials are decorated with Y_2O_3 nanoparticles by mechanical alloying in a planetary mill and followed by consolidation by the laser additive manufacturing process of laser powder bed fusion (L-PBF). While dense specimens (>99.5%) of reinforced and nonreinforced alloys can be manufactured, oxide dispersion-strengthened alloys additionally exhibit homogeneously distributed oxide nanoparticles enriched in yttrium and chromium next to Cr_2Nb precipitates present in all alloys examined. Higher niobium contents result in moderate increase of the Vickers hardness of approx. 10 HV0.3, while the homogeneously dispersed nanometer-sized oxide particles lead to a pronounced increase of approx. 30 HV0.3 in material strength compared to their nonreinforced counterparts.

Keywords: oxide dispersion strengthening; ODS; copper–chromium–niobium; laser additive manufacturing; laser powder bed fusion



Citation: Wilms, M.B.; Rittinghaus, S.-K. Laser Additive Manufacturing of Oxide Dispersion-Strengthened Copper–Chromium–Niobium Alloys. *J. Manuf. Mater. Process.* **2022**, *6*, 102. <https://doi.org/10.3390/jmmp6050102>

Academic Editors: Antonio Riveiro and Rafael Comesaña

Received: 19 July 2022

Accepted: 8 September 2022

Published: 16 September 2022

Publisher's Note: MDPI stays neutral with regard to jurisdictional claims in published maps and institutional affiliations.



Copyright: © 2022 by the authors. Licensee MDPI, Basel, Switzerland. This article is an open access article distributed under the terms and conditions of the Creative Commons Attribution (CC BY) license (<https://creativecommons.org/licenses/by/4.0/>).

1. Introduction

Copper is an indispensable material with a wide field of applications in various engineering sectors, such as automotive, aerospace, electronics, and power generation. The versatility of copper and its alloys is commonly attributed to the unique physical properties of high thermal and electrical conductivity. The utilization of copper alloys as heat-transfer media in high-performance components in aerospace [1–4] and power-generation applications [4–7] requires the development of copper alloys with both high strength and high thermal conductivity. Increasing strength by solid solution strengthening requires significant amounts of additional alloying elements, which drastically decreases the thermal conductivity of copper alloys. Among others systems, e.g., Cu–Ni–Mn [8], Cu–Ag [9], Cu–Co [10], Cu–Mg [11,12] and Cu–Fe–P [13], alloy concepts based on the binary Cu–Cr and Cu–Zr systems have been considered for the development of highly conductive high-strength copper alloys [14], which are interesting because they do not contain highly toxic beryllium. [15]. This is due to the extremely low room temperature solubility of chromium [16] and zirconium in copper at room temperature, resulting in the precipitation of Cr-rich particles [14] and Cu_5Zr precipitates [14,17–19]. Among others, the commercial copper alloys AMZIRC [14,20], CuCr1Zr, and NARloy-Z [20] are based on these developments. The alloys GRCop-84 and GRCop-42, both developed by NASA [20], are based on the ternary Cu–Cr–Nb system, offering higher strength and improved creep properties than the alloys NARloy-Z and AMZIRC by the formation of C15 structured Cr_2Nb laves phases [14,20–25]. The high affinity of Cr and Nb in combination with low

solubility in the copper matrix at room temperature allow the creation of a pure Cu matrix with dispersed Cr_2Nb phases [26,27] after heat treatment [28]. The remarkable creep properties [29] are attributed to the lack of coarsening of the Cr_2Nb phase in the copper matrix [30]. Creep properties are believed to be further improved by the concept of oxide-dispersion strengthening (ODS), where nanoscale oxide particles are dispersed in the metallic matrix. The alloy family of GlidCop [31,32], based on the dispersion of temperature-resistant nanoscale oxides, such as aluminum oxide (Al_2O_3) [14,33–35] and yttrium oxide (Y_2O_3) [36–39], offers increased strength, particularly in high-temperature atmospheres, and inhibits recrystallization mechanisms [40] without significantly reducing electrical conductivity [41]. GRCop (Cu-Cr-Nb), novel Cu-Cr-Nb-Zr [42,43], and GlidCop (ODS copper alloys) [44] are conventionally manufactured via powder metallurgical or rapid solidification manufacturing processes [45–48], such as additive manufacturing processes [34,49] due to aggregation during the molten stage of Cr and Nb in GRCop alloys or oxide nanoparticles in GlidCop alloys, respectively.

Additive manufacturing processes offer near-net-shape fabrication of complex structures in addition to extremely high solidification conditions. While additive manufacturing of ODS steels using laser-based [50] or electron beam-based [51] additive manufacturing processes have already been demonstrated, additive manufacturing of oxide dispersion-strengthened copper alloys only in singular studies [52–54] typically results in highly porous structures [52]. This may be attributed to difficult processing of copper and its alloys, due to its low absorption for near-infrared wavelengths [55] and high specific thermal conductivity leading to unstable melt pool behavior [56], frequently resulting in high porosities [57–61] lack of fusion [57,59,62,63] and oxide formation [64] in printed copper components.

Different strategies for processing copper materials, such as reducing the particle sizes used [65–67], coating of copper powder particles with native oxide layers [68,69], nickel [70] and carbon [71], the utilization of alternative laser wavelengths in the visible spectrum of green [72–74] and blue light [75] and pulsed laser systems [76], have been examined to improve the processability of copper alloys in laser additive manufacturing processes. Cu-Cr-based alloys have established themselves as high-strength and highly conductive with low alloy content and hardenable by the formation of Cr precipitation [77–79]. The additional introduction of Zr allows the formation of nanoscale Zr-rich precipitates during aging heat treatments [80–84]. Moreover, the formation of Zr-O structures is observed [85,86], leading to the hypothesis that Zr may be used to capture residual oxygen introduced by the powder material or the process atmosphere. Cu-Cr-Nb alloys are also increasingly being manufactured with the laser additive manufacturing technologies of L-DED [87–89] and L-PBF [90–95], allowing the manufacturing of dense and defect-free parts with outstanding mechanical properties [4,91,96].

However, significant coarsening of Cr_2Nb precipitations is observed in high-temperature environments [30,92], resulting in rapid degradation of the mechanical properties. In this work, we introduce nanoscale yttrium oxide nanoparticles, which are known to stabilize the microstructure and thus material strength up to high temperatures [97]. It is hypothesized that the introduction of nanoscale oxide particles may allow the increase of the service temperatures from approx. 700 °C for GRCop alloys [32] up to 800 °C for dispersion-strengthened copper alloys [98] without reducing conductive properties [99]. We chose Y_2O_3 as reinforcement phase due to its higher thermodynamic stability than commonly used Al_2O_3 in GlidCop alloys [100] and select two Cu-Cr-Nb alloys with different niobium contents to study the influence of increased niobium contents on the formation of Cr_2Nb precipitates and the chemistry of the introduced yttrium oxide nanoparticles, potentially forming cubic-structured Y_3NbO_7 , as observed in stainless steels [101]. With this approach, we combine the concepts of precipitation-strengthened GRCop and oxide dispersion-strengthened GlidCop families to develop a high-strength, high-temperature-resistant, and highly conductive copper alloy using the AM process of L-PBF.

2. Materials and Methods

2.1. Powder Preparation

Two Cu-Cr-Nb powder materials with the chemical compositions shown in Table 1 are manufactured via vacuum inert gas atomization (VIGA) using argon gas. Both powder materials are sieved to a particle size fraction of 15–45 μm prior to L-PBF processing. Manufacturing of ODS variants from both alloys with additions of 0.5 wt.% nanoscale Y_2O_3 (abcr GmbH, Karlsruhe, Germany) requires the fabrication of composite powder materials with oxide nanoparticles attached to micrometer-sized copper particles. Thus, mechanical alloying (MA) is used to manufacture composite powders and performed in a Pulverisette 4 classic line planetary mill (Fritsch GmbH, Idar-Oberstein, Germany) using milling containers and grinding balls (BPR: 5) with a diameter of 5 mm, both made from yttrium-stabilized zirconia (YSZ). The milling procedure is conducted under full argon atmosphere to avoid extensive oxidation of the copper powder particles in three alternating milling (20 min) and pause intervals (10 min) to allow cooling of the powder material.

Table 1. Nominal chemical composition of the Cu-Cr-Nb powder materials in wt.%.

Alloy 1	Cu Balance	Cr 3.3	Nb 0.5
Alloy 2	Cu Balance	Cr 3.3	Nb 1.5

2.2. Laser Powder Bed Fusion (L-PBF)

Laser powder bed fusion is conducted using a custom laboratory-scaled L-PBF machine equipped with a YLR1000WC single-mode fiber laser system (IPG Laser GmbH, Burbach, Germany) emitting laser radiation with a wavelength of 1070 nm. A Gaussian beam profile with a beam diameter of approx. 80 μm in the focal plane is created by a galvanometer scanner hurrySCAN20 (SCANLAB GmbH, Puchheim, Germany) coupled with an f-theta lens with a focal length of 255 mm. A schematic of the setup of the machine is depicted in Figure 1a.

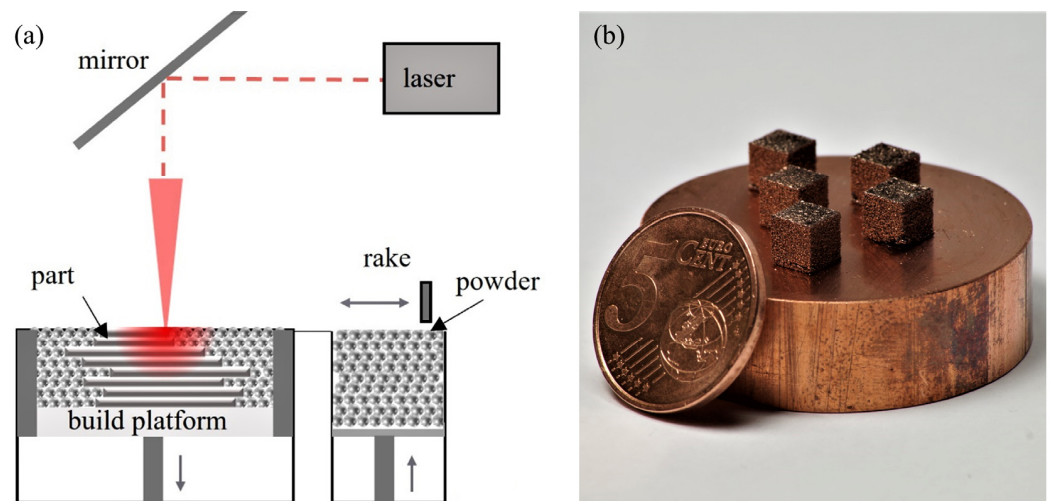


Figure 1. (a) Schematic depiction of the L-PBF machine setup. (b) Photograph of five printed specimen of Cu-3.3Cr-0.5Nb-0.5 Y_2O_3 material on a copper substrate.

L-PBF processing is conducted in a full argon atmosphere (residual oxygen < 10 ppm) with a slight overpressure of approx. 60 mbar compared to ambient atmosphere. Cubic samples (5 mm³) are manufactured on a CuCr1Zr (CW106C) substrate material with a layer-wise rotating stripe scan strategy (34° per layer) using a hatch distance (h_s) of 120 μm and a layer thickness (t_L) of 30 μm . The used laser power (P_L) of 400 W and scan speed (v_s) of 800 mm/s allow the calculation of the volume energy density (VED) to 138.89 J/mm³.

The process parameters are selected based on the process parameter study by Ren et al. [96]. The volume energy density is calculated using (1) [102]. Five specimens of each material are printed (cf. Figure 1b).

$$VED = \frac{P_L}{v_s h_s t_L} \quad (1)$$

Identical process parameter sets are applied to all powder materials processed and are summarized in Table 2.

Table 2. Process parameters for L-PBF processing of Cu-Cr-Nb samples and their reinforced counterparts.

Process Parameter	Unit	Value	Process Parameter	Unit	Value
Laser power	W	400	Hatch rotation	°	34
Scan speed	mm/s	800	Scan strategy	-	Stripes
Hatch distance	µm	120	Residual oxygen	ppm	<10
Layer thickness	µm	30	VED	J/mm ³	138.89

2.3. Characterization Methods

Printed samples are examined by standard metallographic procedure including water-cooled cutting parallel to the build direction, grinding with silicon carbide (SiC) paper and subsequent polishing procedure using a 1 µm diamond polishing suspension. The visual identification of different phases and nanoparticles in the printed specimens is aided by an etching procedure prior to scanning electron microscopy (SEM) examination utilizing an aqueous etchant containing 10 g iron(III) chloride (Fe₃Cl) and 20 mL hydrogen chloride (HCl) in 100 mL deionized water at room temperature for approx. 15 s. The relative density of printed specimens is determined on five polished cross sections prior to etching using the image analysis software ImageJ.

SEM for imagery of powder particles is conducted on a Leo 1455VP (Carl Zeiss Microscopy Deutschland GmbH, Oberkochen, Germany) in secondary electron (SE) mode using an acceleration voltage of 20 kV. SEM images of printed specimens are performed on an Apreo 2C (Thermo Fisher Scientific, Hillsboro, OR, USA) in SE mode and backscattered electron (BSE) mode with 10 kV acceleration voltage. The determination of chemical compositions is performed by energy-dispersive spectroscopy (EDS) measurements with a Bruker XFlash 6L100 detector integrated in the Apreo 2C SEM system.

Hardness measurements are conducted on an automated hardness tester Carat 930 (ATM Qness GmbH, Mammelzen, Germany) in Vickers mode (HV0.3). A regular grid of 6 × 6 indents per sample with a constant distance of 500 µm is performed.

3. Results and Discussion

3.1. Powder Characterization

Both gas-atomized Cu-Cr-0.5Nb (Figure 2a) and Cu-Cr-1.5Nb (Figure 2b) powder materials are characterized by a predominantly spherical morphology with only few particles showing aspheric morphology. The powder particles show a smooth surface with sporadically present satellite particles attached to the powder particles.

The Cu-3.3Cr-1.5Nb powder material (Figure 2b) shows a comparably high fraction of satellites, which are regularly encountered in gas-atomized powder materials [103], showing that an increased niobium content influences the gas atomization process. The pronounced formation of satellites might stem from the higher superheat of the copper melt necessary for gas atomization [104], due to higher liquidus temperature with increasing niobium content [105].

After mechanical alloying, the circularity of the gas-atomized powder particles decreases and flake-like powder particles (indicated by the yellow arrow in Figure 3a) are observed occasionally, which are frequently found in mechanically alloyed powder materials [106,107]. Additionally, the surface of the powder particles appears to be rougher, which presumably stems from the fracturing and cold-welding events during mechanical alloying

processes [108]. Mechanically alloyed powder particles are covered with white-appearing particles (Figure 3a,b). Using EDS measurements, enrichments of yttrium and oxygen can be detected, proving the successful deposition of Y_2O_3 or related compound nanoparticles on the surface of the Cu-Cr-Nb powder particles (Table 3).

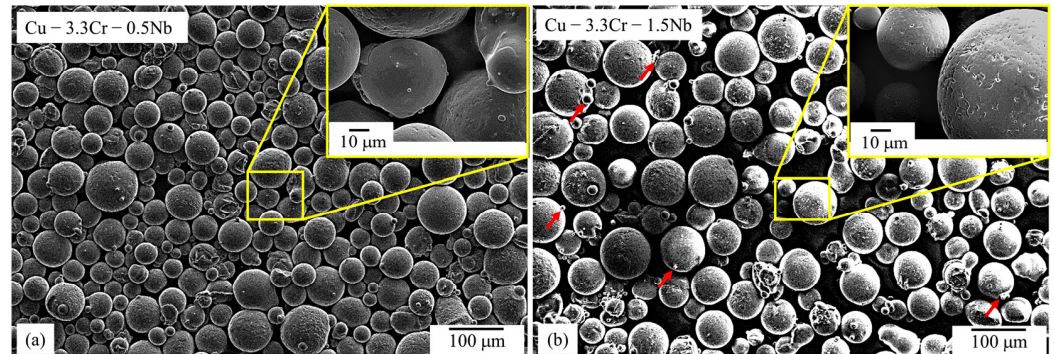


Figure 2. SEM images (SE mode) of gas-atomized powder particles with superimposed SEM image with higher magnification: (a) Cu-3.3Cr-0.5Nb alloy. (b) Cu-3.3Cr-1.5Nb alloy.

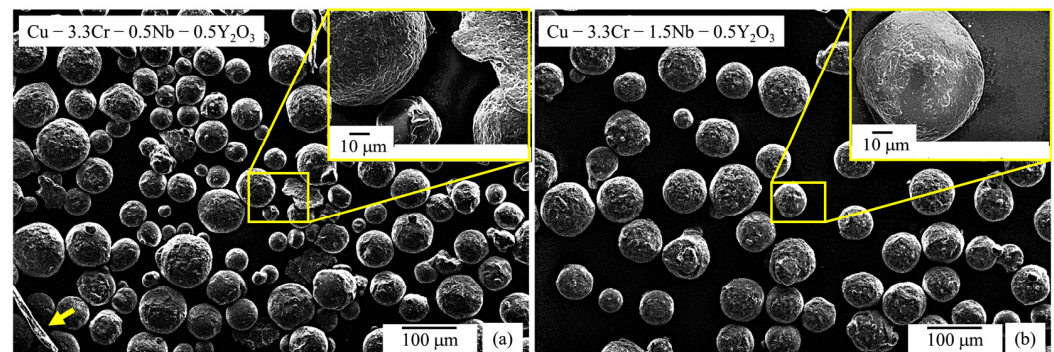


Figure 3. SEM images (SE mode) of mechanically alloyed powder particles with superimposed SEM image with higher magnification: (a) Cu-3.3Cr-0.5Nb alloy. (b) Cu-3.3Cr-1.5Nb alloy.

Table 3. Chemical composition (in wt.%) of the surface of the mechanically alloyed powder depicted in Figure 2a,b. Averaged values from single-point measurements on 15 randomly selected powder particles. GA: gas-atomized, MA: mechanically alloyed.

Alloy	Powder State	Cu	Cr	Nb	Y	O
Cu-3.3Cr-0.5Nb	GA	Balance	2.82	0.77	-	1.77
Cu-3.3Cr-0.5Nb-0.5Y ₂ O ₃	MA	Balance	3.73	1.15	4.91	3.18
Cu-3.3Cr-1.5Nb	GA	Balance	3.55	1.86	-	2.58
Cu-3.3Cr-1.5Nb-0.5Y ₂ O ₃	MA	Balance	3.31	1.78	4.02	2.47

Overall, a predominantly spherical particle morphology of both gas atomized powder materials was retained after mechanical alloying (Figure 3a,b) and thus the mechanically alloyed powder materials exhibit satisfactory flowability for L-PBF processing.

The presence of yttrium-rich oxide nanoparticles is believed to allow the utilization of substantially lower VED compared to other studies, with 277.78 J/mm³ [60] to produce dense specimens in this study (Table 2) by increasing the absorptivity for the used laser radiation [109] by multiple reflections [110]. EDS measurements on the powder particles surface additionally indicate an inhomogeneous distribution of chromium and niobium in the copper matrix of the gas-atomized and mechanically alloyed powder particles, which is confirmed by EDS maps of the powder particles' cross sections (Figure 4a–d). Comparable inhomogeneities were also observed by Seltzman et al. [4,91], but do not result in detrimental effects on the L-PBF printing process or homogeneous distribution of Cr₂Nb laves phase in the printed copper matrix [91].

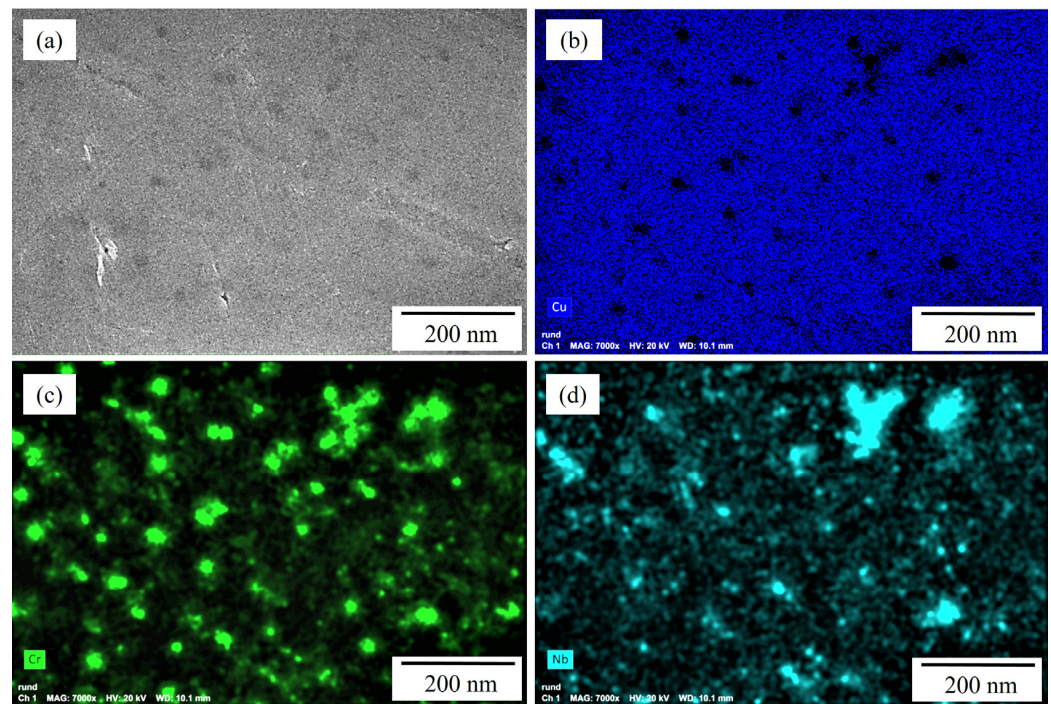


Figure 4. EDS maps of cross sections of randomly selected Cu-3.3Cr-1.5Nb powder particles in gas-atomized state: (a) BSE image showing the presence of darker-appearing particles indicating local enrichment of elements with higher atomic number. EDS maps of copper (b), chromium (c) and niobium (d) confirm the local enrichment of chromium and niobium of dark-appearing particles.

3.2. Microstructure

3.2.1. Unreinforced Cu-Cr-Nb Alloys

Figure 5 provides SEM images of cross sections of the unreinforced Cu-3.3Cr-0.5Nb (Figure 5a,b) and Cu-3.3Cr-1.5Nb (Figure 5c,d) in the as-printed state. The microstructure is characterized by a layered structure, showing the melt pool boundaries of the printed layers, characteristic of AM printed parts [111]. The printed cubic structures are found to be almost defect-free, exhibiting no cracks and low porosities, resulting in a relative density of $99.7\% \pm 0.2\%$ and $99.4\% \pm 0.3\%$ respectively. These results are in accordance with findings of Seltzman et al. [4,91] and Ren et al. [96], both demonstrating the defect-free manufacturing of GRCo-84 and Cu-1.93Cr-0.74Nb alloy. Two homogeneously distributed populations of nanosized particles, indicated by yellow and red arrows in Figure 5b,d, are observed in both unreinforced specimens, which can be distinguished by their respective size.

The larger particles, which are marked by yellow arrows (Figure 5b,d) have an approximate size of 100–300 nm and are found to be enriched in chromium. In contrast, the smaller nanoparticle population (red arrows) with sizes below 100 nm shows high amounts of chromium and niobium. This correlates with particle size found in L-PBF processed GRCo-84 alloy of 85–200 nm [4,91]. However, due to the small size of both nanoparticle species, EDS measurements were performed on sporadically found clusters of the respective nanoparticle species and therefore large amounts of copper are detected. (Table 4).

The presence of Cr-rich- [14,26] and Cr-Nb-rich precipitates [22,24–28] are frequently observed in Cu-Cr-Nb alloys. The latter particles may correspond to Cr_2Nb laves phase, which is also found together with Cr-rich precipitates in laser-directed energy deposition (L-DED) processed Cu-3.4Cr-0.6Nb (at.%) alloy [88]. Interestingly, no Cr-rich precipitates are observed in L-PBF processed GRCo-84 alloy [4,88], which contradicts the findings of Yang et al. [112,113] showing faster precipitation of L_{12} -structured Cu_3Cr from pure Cr precipitates compared to Cr_2Nb laves phases. However, it is also shown that precipitation

of Cr₂Nb laves phases is enabled at temperatures exceeding 600 °C, consuming Cr-rich precipitations upon formation of Cr₂Nb [107]. We hypothesize that at a fixed Cr/Nb ratio of 2 in combination with high melt pool temperatures of melt pools formed in L-PBF processes favor direct precipitation of Cr₂Nb from the supersaturate copper matrix or lead to full transformation of Cr-rich precipitates to Cr₂Nb laves phases. Consequently, exceeding the ratio of Cr/Nb of 2 will allow excess Cr to remain in the copper matrix as Cr or Cu₃Cr precipitates.

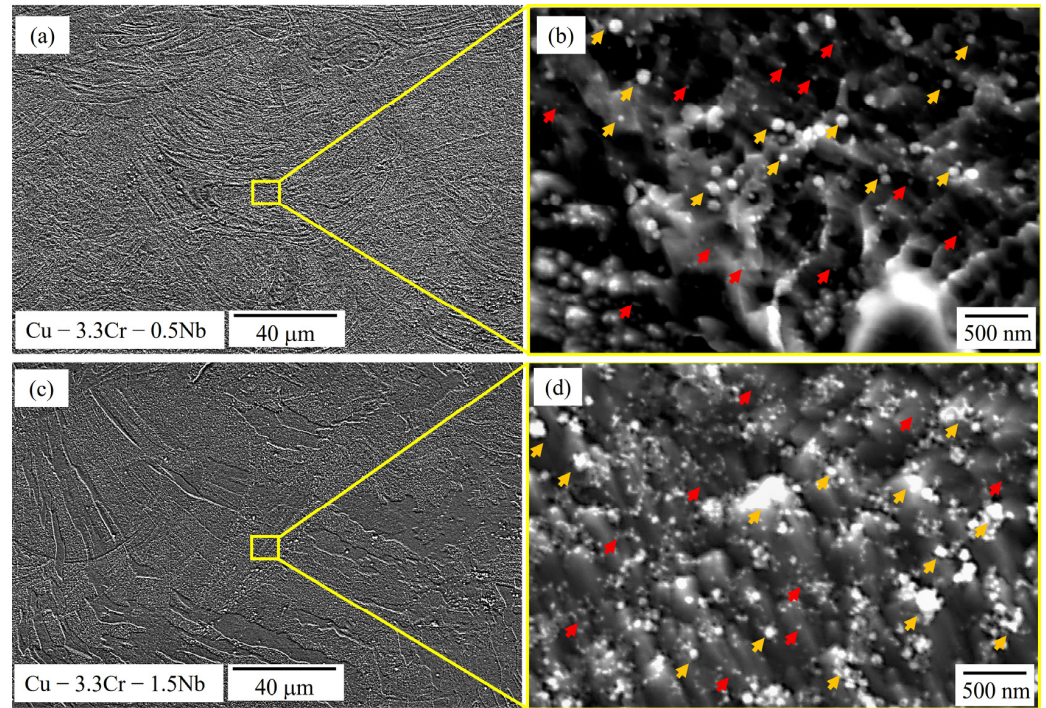


Figure 5. SEM images (SE mode) of Cu-3.3Cr-0.5Nb alloy in low (a) and high magnification (b) showing the presence of different precipitates (red and yellow arrows). SEM images (SE mode) of Cu-3.3Cr-1.5Nb alloy in low (c) and high magnification (d) showing the presence of different precipitates (red and yellow arrows).

Table 4. Chemical composition (in wt.%) of unreinforced specimens determined by EDS. Values are averaged over 12 single-point measurements on occasionally found clusters or larger particles of the respective nanoparticle species.

Alloy	Particle Species	Cu	Cr	Nb	Y	O
Cu-3.3Cr-0.5Nb	Red arrows	Balance	16.86	9.12	-	3.01
	Yellow arrows	Balance	37.44	-	-	1.24
Cu-3.3Cr-1.5Nb	Red arrows	Balance	23.73	12.33	-	4.70
	Yellow arrows	Balance	48.44	-	-	2.39

3.2.2. Y₂O₃-Reinforced Cu-Cr-Nb Alloys

In Figure 6 SEM images of the reinforced Cu-3.3Cr-0.5Nb-0.5Y₂O₃ (Figure 6a,b) and Cu-3.3Cr-1.5Nb-0.5Y₂O₃ (Figure 6c,d) are shown. No apparent differences regarding grain morphology or size are observable compared to the unreinforced specimen in Figure 4. However, on a lower scale significant differences in the microstructure evolution become apparent: a large number of sub-100 nm-sized nanoparticles are distributed within the metallic matrix. However, EDS measurements of nanoparticle clusters (Table 5) reveal the presence of two nanoparticle species, marked with yellow and red arrows, respectively (Figure 6b,d). Smaller particles are marked with red arrows and correspond to Cr-Nb-rich precipitates, which were observed in the unreinforced specimen.

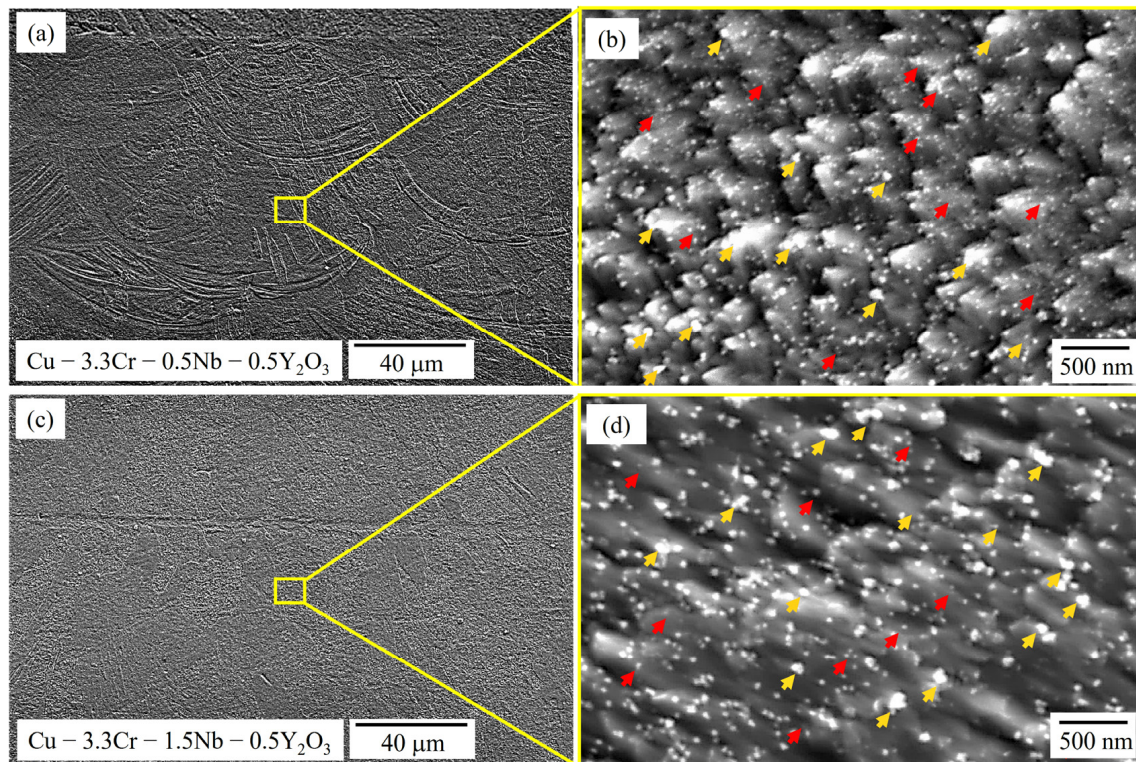


Figure 6. SEM images of oxide-reinforced Cu-3.3Cr-0.5Nb alloy in low (a) and high magnification (b) showing the presence of precipitates (red arrows) and dispersoids (yellow arrows). SEM images of oxide-reinforced Cu-3.3Cr-1.5Nb alloy in low (c) and high magnification (d) showing the presence of precipitates (red arrows) and dispersoids (yellow arrows).

Table 5. Chemical composition (in wt.%) of reinforced specimens determined by EDS. Values are averaged over 12 single-point measurements on occasionally found clusters or larger particles of the respective nanoparticle species.

Alloy	Particle Species	Cu	Cr	Nb	Y	O
Cu-3.3Cr-0.5Nb-0.5Y ₂ O ₃	Red arrows	Balance	21.86	7.87	-	4.11
	Yellow arrows	Balance	27.24	-	14.04	7.24
Cu-3.3Cr-1.5Nb-0.5Y ₂ O ₃	Red arrows	Balance	24.93	9.85	-	2.68
	Yellow arrows	Balance	37.13	-	11.07	8.42

Interestingly, the larger nanoparticles, which are marked with yellow arrows, are enriched in yttrium, chromium and oxygen. Thus, the addition of Y₂O₃ nanoparticles seems to promote the formation of complex oxide compounds. The found chromium-rich yttrium oxide nanoparticles may be attributed to the monoclinic-structured compound of YCrO₃, which is frequently observed in Cr-alloyed ODS steels [114–116] and nickel-based ODS alloys [117]. The formation reaction can be described according to (2) [118].



The proposed formation reaction of YCrO₃ (1) implies the introduction of additional oxygen to the process zone. While the gas atmosphere during L-PBF processing only contains negligible amounts of oxygen (Table 2), oxygen might be introduced into the printing process from the powder material. Copper powder handled in air is known to form an oxide layer, consisting of CuO [52,53], and thus might carry oxygen into the printing process to provide oxygen to form YCrO₃. The EDS measurements performed on

the powder particles' surface confirms the presence of oxygen, presumably bound as a thin oxide layer (Table 3).

3.3. Mechanical Properties

Mechanical properties of the printed oxide-reinforced materials and their unreinforced counterparts are characterized by hardness measurements. In Figure 7, representative hardness maps of printed specimens of Cu-3.3Cr-0.5Nb (Figure 7a) and Cu-3.3Cr-1.5Nb (Figure 7b) are depicted. Both materials are characterized by a relatively moderate hardness of 120–140 HV0.3. The hardness is distributed fairly homogeneous over the printed part with hardness variations up to 15 HV0.3. Oxide dispersion-strengthened Cu-3.3Cr-0.5Nb (Figure 7c) and Cu-3.3Cr-1.5Nb (Figure 7d) show considerably higher hardness compared to their unreinforced counterparts, which is in accordance with other metallic systems with dispersed oxide nanoparticles [50,119].

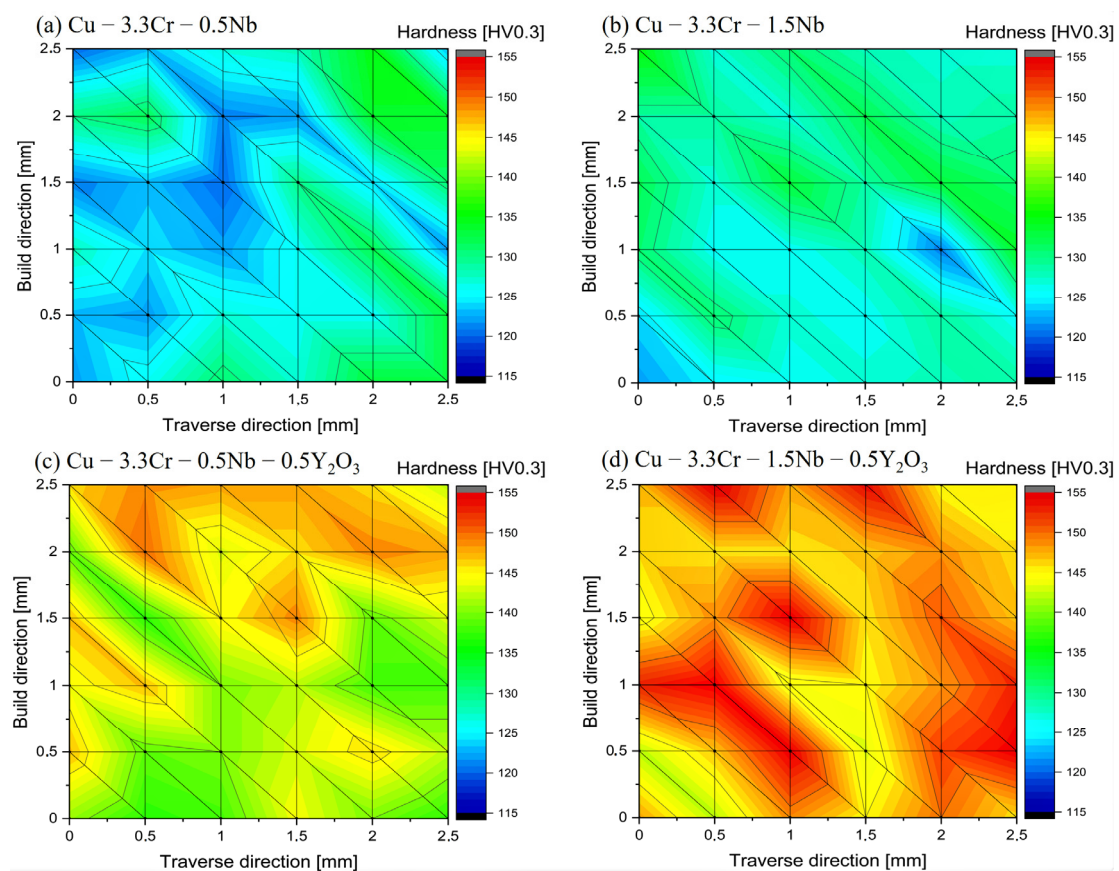


Figure 7. Vickers hardness (HV0.3) maps of manufactured specimens in the as-printed state. (a) Cu-3.3Cr-0.5Nb. (b) Cu-3.3Cr-1.5Nb. (c) Cu-3.3Cr-0.5Nb-0.5Y₂O₃. (d) Cu-3.3Cr-1.5Nb-0.5Y₂O₃. The hardness between the individual hardness indents is linearly interpolated.

The rather homogeneous nature of the hardness distribution is also reflected by the averaged hardness of the line profiles, shown in Figure 8. Here, the superior hardness levels of oxide-dispersed material compared to the raw copper alloys becomes apparent. Additionally, higher niobium contents are also favorable for higher strength, presumably by higher fractions of nanoscale-precipitated Cr₂Nb laves phases, which cannot be resolved with the used SEM system.

Considering the hardness values of extruded [30,120] and L-DED [87] processed Cu-Cr-Nb alloys, L-PBF-manufactured material shows superior hardness despite lower chromium and niobium contents, which typically stems from smaller grains due to higher cooling rates in L-PBF than L-DED or extrusion processes. [50] However, Kini et al. [88] presents notably high hardness values (approx. 146 HV) for L-DED-manufactured Cu-3.4Cr-0.6Nb (at.%)

material, due to in situ precipitation of Cr_2Nb laves particles by intrinsic heat treatment (IHT) mechanisms, frequently observed in L-DED processes [121–124]. The higher fraction of precipitated Cr_2Nb and Cr-rich phases directly leads to increased hardness. Thus, it is hypothesized that a subsequent aging procedure of L-PBF manufactured material will result in further increase in the hardness superior to L-DED-manufactured counterparts.

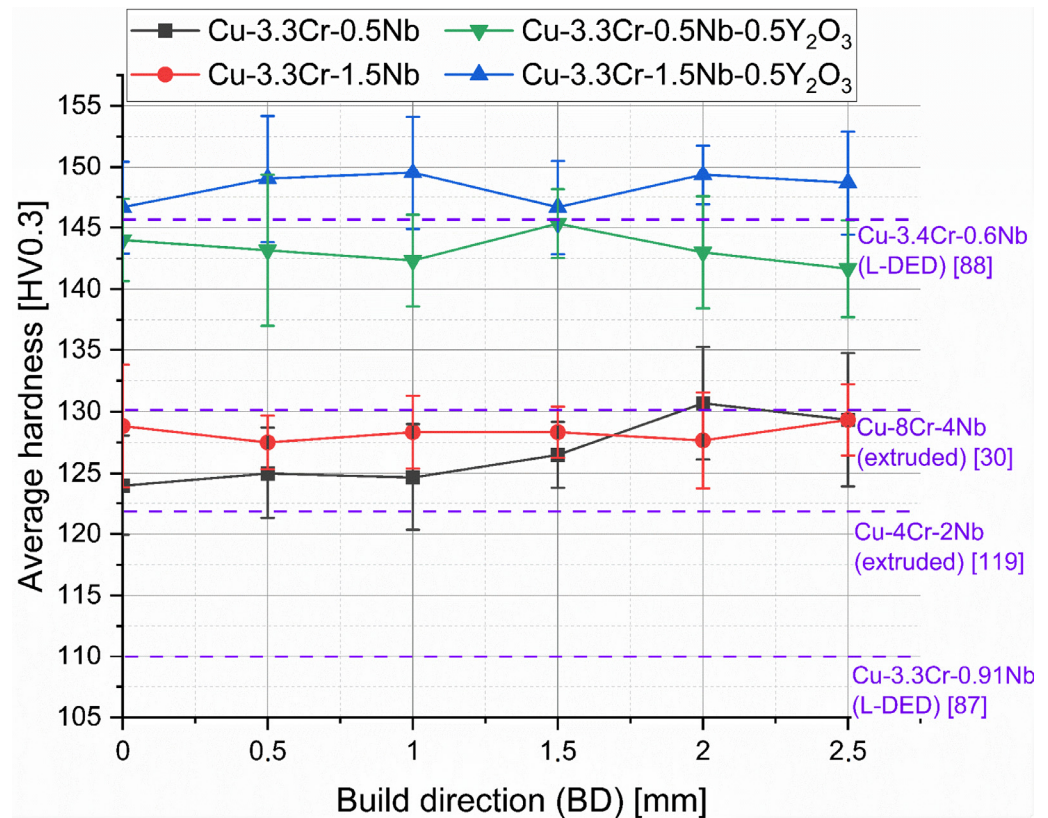


Figure 8. Hardness line profiles of manufactured specimen of Cu-3.3Cr-0.5Nb (black line), Cu-3.3Cr-1.5Nb (red line), Cu-3.3Cr-0.5Nb-0.5Y₂O₃ (green line), and Cu-3.3Cr-1.5Nb-0.5Y₂O₃ (blue line). Hardness values of Cu-Cr-Nb alloys manufactured by extrusion and laser directed energy deposition (L-DED) are shown in purple with their respective reference.

4. Conclusions

In the present study, we demonstrated the feasibility of printing oxide dispersion-strengthened Cu-Cr-Nb alloys by the additive manufacturing process of laser powder bed fusion. The addition of nanoscale Y₂O₃ results in a complex microstructure with populations of Cr- and Nb-enriched nanoparticles next to Cr-rich yttrium oxide nanoparticles, homogeneously dispersed in the metallic copper matrix. The evolution of both nanoparticle species by addition of Y₂O₃ led to a remarkable increase of the hardness compared to their unreinforced counterparts. Future studies will include in-depth microstructural characterization including TEM investigations to clarify the nanoparticle chemistry and extensive mechanical characterizations using tensile test and creep tests. Additionally, modifications of the alloy system towards refined oxide nanoparticles as well as the effect of higher oxide particle contents are topics for future studies.

Author Contributions: Conceptualization, M.B.W. and S.-K.R.; methodology, M.B.W. and S.-K.R.; validation, M.B.W. and S.-K.R.; formal analysis, M.B.W.; investigation, M.B.W. and S.-K.R.; resources, M.B.W. and S.-K.R.; data curation, M.B.W.; writing—original draft preparation, M.B.W.; writing—review and editing, M.B.W. and S.-K.R.; visualization, M.B.W. All authors have read and agreed to the published version of the manuscript.

Funding: This research received no external funding.

Data Availability Statement: All data generated or analyzed during this study are included in this published article.

Acknowledgments: We thank Herbert Horn-Solle for his support in conducting SEM imagery and EDS examinations.

Conflicts of Interest: The authors declare no conflict of interest.

References

1. Blakey-Milner, B.; Gradl, P.; Snedden, G.; Brooks, M.; Pitot, J.; Lopez, E.; Leary, M.; Berto, F.; du Plessis, A. Metal additive manufacturing in aerospace: A review. *Mater. Des.* **2021**, *209*, 110008. [[CrossRef](#)]
2. Gradl, P.; Tinker, D.C.; Park, A.; Mireles, O.R.; Garcia, M.; Wilkerson, R.; Mckinney, C. Robust metal additive manufacturing process selection. *J. Mater. Eng. Perform.* **2022**, *31*, 6013–6044. [[CrossRef](#)]
3. Gradl, P.R.; Protz, C.S.; Zagorski, K.; Doshi, V.; McCallum, H. Additive manufacturing and hot-fire testing of bimetallic GRCop-84 and C-18150 channel-cooled combustion chambers using powder bed fusion and Inconel 625 hybrid directed energy deposition. In Proceedings of the 55th AIAA/SAE/ASEE Joint Propulsion Conference, Indianapolis, IN, USA, 19–21 August 2019. [[CrossRef](#)]
4. Seltzman, A.H.; Wukitch, S.J. Fracture characteristics and heat treatment of laser powder bed fusion additively manufactured GRCop-84 copper. *Mater. Sci. Eng. A* **2021**, *827*, 141690. [[CrossRef](#)]
5. Butterworth, G.J.; Forty, C.B.A. A survey of the properties of copper alloys for use as fusion reactor materials. *J. Nucl. Mater.* **1992**, *189*, 237–276. [[CrossRef](#)]
6. Zinkle, S.J. Applicability of copper alloys for DEMO high heat flux components. *Phys. Scr.* **2016**, *T167*, 014004. [[CrossRef](#)]
7. Singer, F.; Deisenroth, D.C.; Hymas, D.M.; Dessiatoun, S.V.; Ohadi, M.M. Additively manufactured copper components and composite structures for thermal management applications. In Proceedings of the 16th IEEE Intersoc. Conf. Thermal and Thermomechanical Phenomena in Electronic Systems, Orlando, FL, USA, 30 May–2 June 2017. [[CrossRef](#)]
8. Altenberger, I.; Kuhn, H.-A.; Müller, H.R.; Mhaede, M.; Gholami-Kermanshahi, M.; Wagner, L. Material properties of high-strength beryllium-free copper alloys. *Int. J. Mater. Prod. Techn.* **2015**, *50*, 124–146. [[CrossRef](#)]
9. Yang, H.-Y.; Ma, Z.-C.; Lei, C.-H.; Meng, L.; Fang, Y.-T.; Liu, J.-B.; Wang, H.-T. High strength and high conductivity Cu alloys: A review. *Techn. Sci.* **2020**, *63*, 2505–2517. [[CrossRef](#)]
10. Geng, Y.; Ban, Y.; Li, X.; Zhang, Y.; Jia, Y.; Tian, B.; Zhou, M.; Liu, Y.; Volinsky, A.A.; Song, K.; et al. Excellent mechanical properties and high electrical conductivity of Cu-Co-Si-Ti alloy due to multiple strengthening. *Mater. Sci. Eng. A* **2021**, *821*, 141639. [[CrossRef](#)]
11. Tong, Y.-X.; Li, S.-Y.; Zhang, D.-T.; Li, L.; Zheng, Y.-F. High strength and high electrical conductivity CuMg alloy prepared by cryorolling. *Trans. Nonferr. Met. Soc. China* **2019**, *29*, 595–600. [[CrossRef](#)]
12. Maki, K.; Ito, Y.; Matsunaga, H.; Mori, H. Solid-solution copper alloys with high strength and high electrical conductivity. *Scr. Mater.* **2013**, *68*, 777–780. [[CrossRef](#)]
13. Zhang, X.; Zhang, Y.; Tian, B.; Song, K.; Liu, P.; Jia, Y.; Chen, X.; An, J.; Zhao, Z.; Liu, Y.; et al. Review of nano-phase effects in high-strength and conductivity copper alloys. *Nanotechn. Rev.* **2019**, *8*, 383–395. [[CrossRef](#)]
14. Minneci, R.P.; Lass, E.A.; Bunn, J.R.; Choo, H.; Rawn, C.J. Copper-based alloys for structural high-heat-flux applications: A review of development, properties, and performance of Cu-rich Cu-Cr-Nb alloys. *Int. Mater. Rev.* **2021**, *66*, 394–425. [[CrossRef](#)]
15. Akada, T.; Izumida, H.; Watanabe, T.; Iwamoto, K. High-strength and high-conductive material to replace beryllium-copper alloys. *SEI Techn. Rev.* **2017**, *84*, 156–159.
16. Raabe, D.; Ohsaki, S.; Hono, K. Mechanical alloying and amorphization in Cu-Nb-Ag in situ composite wires studied by transmission electron microscopy and atom probe tomography. *Acta Mater.* **2009**, *57*, 5254–5263. [[CrossRef](#)]
17. Liang, D.; Wang, N.; Wang, Y.; Liu, Z.; Fu, Y. Effects of Zr, Y on the microstructure and properties of fast-cast Cu-0.5Y-xZr (wt.%) alloys. *Metals* **2019**, *9*, 1084. [[CrossRef](#)]
18. Li, R.; Kang, H.; Chen, Z.; Fan, G.; Zou, C.; Wang, W.; Zhang, S.; Lu, Y.; Jie, J.; Cao, Z.; et al. A promising structure for fabrication high strength and high electrical conductivity copper alloys. *Sci. Rep.* **2016**, *6*, 20799. [[CrossRef](#)]
19. Zhou, C.; Chen, Z.; Guo, E.; Kang, H.; Fan, G.; Wang, W.; Li, R.; Zhang, S.; Wang, T. A nano-micro dual-scale particulate-reinforced copper matrix composite with high strength, high electrical conductivity and superior wear resistance. *RSC Adv.* **2018**, *8*, 30777. [[CrossRef](#)]
20. de Groh III, H.C.; Ellis, D.L.; Loewenthal, W.S. Comparison of GRCop-84 to other Cu alloys with high thermal conductivities. *J. Mater. Eng. Perform.* **2008**, *17*, 594–606. [[CrossRef](#)]
21. Li, W.-Y.; Guo, X.-P.; Verdy, C.; Dembinski, L.; Liao, H.L.; Coddet, C. Improvement of microstructure and property of cold-sprayed Cu-4 at.%Cr-2 at.%Nb alloy by heat treatment. *Scr. Mater.* **2006**, *55*, 327–330. [[CrossRef](#)]
22. Yang, X.H.; Wang, C.D.; Yang, L.; Zou, J.T.; Xiao, P.; Liang, S.H. Effects of Nb addition and different cooling methods on microstructures and properties of Cu-Cr alloys. *J. Mater. Eng. Perform.* **2020**, *29*, 5008–5017. [[CrossRef](#)]
23. Li, W.-Y.; Guo, X.-P.; Verdy, C.; Dembinski, L.; Liao, H.L.; Coddet, C. Effect of vacuum heat treatment on microstructure and microhardness of cold sprayed Cu-4Cr-2Nb alloy coating. *Trans. Nonferr. Met. Soc. China* **2006**, *16*, 203–208. [[CrossRef](#)]
24. Shukla, A.K.; Narayana Murty, S.V.S.; Suresh Kumar, R.; Mondal, K. Spark plasma sintering of dispersion hardened Cu-Cr-Nb alloy powders. *J. All. Comp.* **2013**, *577*, 70–78. [[CrossRef](#)]

25. Wu, X.; Wang, R.; Peng, C.; Feng, Y.; Cai, Z. Microstructures and elevated temperature properties of rapidly solidified Cu-3Ag-0.5Zr and Cu-3Ag-0.5Zr-0.4Cr-0.35Nb alloys. *J. All. Comp.* **2019**, *803*, 1037–1044. [[CrossRef](#)]
26. Guo, X.; Xiao, Z.; Qiu, W.; Li, Z.; Zhao, Z.; Wang, X.; Jiang, Y. Microstructure and properties of Cu-Cr-Nb alloy with high strength, high electrical conductivity and good softening resistance performance at elevated temperature. *Mater. Sci. Eng. A* **2019**, *749*, 281–290. [[CrossRef](#)]
27. Scannapieco, D.S.; Lewandowski, J.J.; Rogers, R.B.; Ellis, D.L. *In-situ Alloying of GRCop-42 via Additive Manufacturing: Precipitate Analysis*; NASA Technical Reports, TM-20205003857; NASA Glenn Research Center: Cleveland, OH, USA, 2020.
28. Lv, X.; Liu, Z.; Lei, T.; Li, Q.; Ren, Y.; Zhou, X.; Zhang, Z. Effect of heat treatment on Cr2Nb phase and properties of spark plasma sintered Cu-2Cr-1Nb alloy. *Materials* **2020**, *13*, 2860. [[CrossRef](#)]
29. Decker, M.W.; Groza, J.R.; Gibeling, J.C. Creep properties of an extruded copper-8% chromium-4% niobium alloy. *Mater. Sci. Eng. A* **2004**, *369*, 101–111. [[CrossRef](#)]
30. Anderson, K.R.; Groza, J.R.; Dreshfield, R.L.; Ellis, D. High-performance alloy dispersion-strengthened Cu-8 Cr-4 Nb alloy. *Met. Mater. Trans. A* **1995**, *26*, 2197–2206. [[CrossRef](#)]
31. Miller, T.J.; Zinkle, S.J.; Chin, B.A. Strength and fatigue of dispersion-strengthened copper. *J. Nucl. Mater.* **1991**, *179–181*, 263–266. [[CrossRef](#)]
32. Ellis, D.L. *GRCop-84: A High-Temperature Copper Alloy for High-Heat-Flux Applications*; NASA Technical Reports, TM-2005-213566; NASA Glenn Research Center: Cleveland, OH, USA, 2005.
33. Chandrasekhar, S.B.; Sudhakakara Sarma, S.; Ramakrishna, M.; Suresh Babu, P.; Rao, T.N.; Kashyap, B.P. Microstructure and properties of hot extruded Cu-1 wt.% Al₂O₃ nano-composites synthesized by various techniques. *Mater. Sci. Eng. A* **2014**, *591*, 46–53. [[CrossRef](#)]
34. Daoud, A.; Vogt, J.B.; Charkaluk, E.; Bouquerel, J.; Zhang, L.; Biasci, J.-C. Anisotropy effects on the tensile and fatigue behaviour of an oxide dispersion strengthened copper alloy. *Mater. Sci. Eng. A* **2012**, *534*, 640–648. [[CrossRef](#)]
35. Srivatsan, T.S.; Dhana Singh, K.; Troxell, J.D. The tensile behavior of an oxide dispersion strengthened copper-niobium composite. *Mater. Lett.* **1996**, *28*, 423–429. [[CrossRef](#)]
36. Carro, G.; Muñoz, A.; Monge, M.A.; Savoini, B.; Pareja, R.; Ballesteros, C.; Adeva, P. Fabrication and characterization of Y₂O₃ dispersion strengthened copper. *J. Nucl. Mater.* **2014**, *455*, 655–659. [[CrossRef](#)]
37. Aghamiri, S.M.S.; Oono, N.; Ukai, S.; Kasada, R.; Noto, H.; Hishinuma, Y.; Muroga, T. Microstructure and mechanical properties of mechanically alloyed ODS copper alloy for fusion material application. *Nucl. Mater. Ener.* **2018**, *15*, 17–22. [[CrossRef](#)]
38. Martin, U.; Kudashov, D.V.; Heilmair, M.; Oettel, H. Microstructure and deformation behaviour of ultra-fine-grained ODS copper prepared by mechanical alloying. In *High Performance Structures and Materials II*; WIT Press: Southampton, UK, 2004. [[CrossRef](#)]
39. Muñoz, A.; Savoini, B.; Monge, M.A.; Dura, O.J. Fabrication and characterization of Cu reinforced with Y-enriched particles following a novel powder metallurgy route. *Nucl. Mater. Ener.* **2021**, *29*, 101075. [[CrossRef](#)]
40. Mu, Z.; Geng, H.-R.; Li, M.-M.; Nie, G.-L.; Leng, J.-F. Effects of Y₂O₃ on the property of copper based contact materials. *Comp. B* **2013**, *52*, 51–55. [[CrossRef](#)]
41. Shabadi, R.; Avettand-Fènoël, M.N.; Simar, A.; Taillard, R.; Jain, P.K.; Johnson, R. Thermal conductivity in yttria dispersed copper. *Mater. Des.* **2015**, *65*, 869–877. [[CrossRef](#)]
42. Cheng, B.; Wang, L.; Sprouster, D.J.; Trelewicz, J.R.; Zhong, W.; Yang, Y.; Zinkle, S.J.; Snead, L.L. Tailoring microstructure in sintered Cu-Cr-Nb-Zr alloys for fusion components. *J. Nucl. Mater.* **2021**, *551*, 152956. [[CrossRef](#)]
43. Yang, Y.; Wang, L.; Snead, L.; Zinkle, S.J. Development of novel Cu-Cr-Nb-Zr alloys with the aid of computational thermodynamics. *Mater. Des.* **2018**, *156*, 370–380. [[CrossRef](#)]
44. Broyles, S.E.; Zhang, M.; Gibeling, J.C. Influence of annealing on the creep behaviour of GlidCop Al-15. *Mater. Sci. Eng. A* **2020**, *779*, 139112. [[CrossRef](#)]
45. Yamada, T.; Noto, H.; Hishinuma, Y.; Muroga, T.; Nakamura, H. Development of a dispersion strengthened copper alloy using a MA-HIP method. *Nucl. Mater. Ener.* **2016**, *9*, 455–458. [[CrossRef](#)]
46. Shimada, Y.; Mizumoto, M.; Hishinuma, Y.; Ikeda, K.-I.; Yoshida, K.; Noto, H.; Ma, B.; Muroga, T.; Nagai, Y.; Konno, T.J. Microstructural changes of oxide dispersion strengthened copper powders by mechanical alloying. *Fus. Eng. Des.* **2021**, *173*, 112804. [[CrossRef](#)]
47. Ma, B.; Hishinuma, Y.; Noto, H.; Shimada, Y.; Muroga, T. Development of Y₂O₃ dispersion strengthened Cu alloy using Cu₆Y and Cu₂O addition through the MA-HIP process. *Fus. Eng. Des.* **2020**, *161*, 112045. [[CrossRef](#)]
48. Ma, B.; Hishinuma, Y.; Shimada, Y.; Noto, H.; Kasada, R.; Oono, N.; Ukai, S.; Muroga, T. The size dependence of microstructure and hardness on the MA powders for the MA-HIP processed Cu-Y₂O₃ dispersion-strengthened alloys. *Nucl. Mater. Ener.* **2020**, *24*, 100773. [[CrossRef](#)]
49. Ramirez, D.A.; Murr, L.E.; Martinez, E.; Hernandez, D.H.; Martinez, J.L.; Machado, B.I.; Medina, F.; Frigola, P.; Wicker, R.B. Novel precipitate-microstructural architecture developed in the fabrication of solid copper components by additive manufacturing using electron beam melting. *Acta Mater.* **2011**, *59*, 4088–4099. [[CrossRef](#)]
50. Doñate-Buendia, C.; Kürnsteiner, P.; Stern, F.; Wilms, M.B.; Streubel, R.; Kusoglu, I.M.; Tenkamp, J.; Bruder, E.; Pirch, N.; Barcikowski, S.; et al. Microstructure formation and mechanical properties of ODS steels built by laser additive manufacturing of nanoparticle coated iron-chromium powders. *Acta Mater.* **2021**, *206*, 116566. [[CrossRef](#)]

51. Gao, R.; Zeng, L.; Ding, H.; Zhang, T.; Wang, X.; Fang, Q. Characterization of oxide dispersion strengthened ferritic steel fabricated by electron beam selective melting. *Mater. Des.* **2016**, *89*, 1171–1180. [[CrossRef](#)]
52. Pobel, C.R.; Lodes, M.A.; Körner, C. Selective electron beam melting of oxide dispersion strengthened copper. *Adv. Eng. Mater.* **2018**, *20*, 1800068. [[CrossRef](#)]
53. Guschlbauer, R.; Burkhardt, A.K.; Fu, Z.; Körner, C. Effect of oxygen content of pure copper powder on selective electron beam melting. *Mater. Sci. Eng. A* **2020**, *779*, 139106. [[CrossRef](#)]
54. Baitimerov, R.M.; Bykov, V.A. Processing of alumina reinforced copper metal matrix composite by selective laser melting technology. *Solid State Phenom.* **2021**, *316*, 175–180. [[CrossRef](#)]
55. Brandau, B.; Da Silva, A.; Wilsnack, C.; Brueckner, F.; Kaplan, A.F.H. Absorbance study of powder conditions for laser additive manufacturing. *Mater. Des.* **2022**, *216*, 110591. [[CrossRef](#)]
56. Tran, T.Q.; Chinnappan, A.; Lee, J.K.Y.; Loc, N.H.; Tran, L.T.; Wang, G.; Kumar, V.V.; Jayathilaka, W.A.D.M.; Ji, D.; Doddamani, M.; et al. 3D printing of highly pure copper. *Metals* **2019**, *9*, 756. [[CrossRef](#)]
57. Jiang, Q.; Zhang, P.; Yu, Z.; Shi, H.; Wu, D.; Yan, H.; Ye, X.; Lu, Q.; Tian, Y. A review on additive manufacturing of pure copper. *Coatings* **2021**, *11*, 740. [[CrossRef](#)]
58. Constantin, L.; Wu, Z.; Fan, L.; Silvain, J.-F.; Lu, Y.F. Laser 3D printing of complex copper structures. *Addit. Manuf.* **2020**, *35*, 101268. [[CrossRef](#)]
59. Yadav, S.; Paul, C.P.; Jinoop, A.N.; Rai, A.K.; Bindra, K.S. Laser directed energy deposition based additive manufacturing of copper: Process development and material characterizations. *J. Manuf. Proc.* **2020**, *58*, 984–997. [[CrossRef](#)]
60. Tiberto, D.; Klotz, U.E.; Held, F.; Wolf, G. Additive manufacturing of copper alloys: Influence of process parameters and alloying elements. *Mater. Sci. Techn.* **2019**, *35*, 969–977. [[CrossRef](#)]
61. Silbernagel, C.; Gargalis, L.; Ashcroft, I.; Hague, R.; Galea, M.; Dickens, P. Electrical resistivity of pure copper processed by medium-powered laser powder bed fusion additive manufacturing for use in electromagnetic applications. *Addit. Manuf.* **2019**, *29*, 100831. [[CrossRef](#)]
62. Ikeshoji, T.-T.; Nakamura, K.; Yonehara, M.; Imai, K.; Kyogoku, H. Selective laser melting of pure copper. *JOM* **2018**, *70*, 396–400. [[CrossRef](#)]
63. Colopi, M.; Caprio, L.; Demir, A.G.; Previtali, B. Selective laser melting of pure Cu with a 1 kW single mode fiber laser. *Proc. CIRP* **2018**, *74*, 59–63. [[CrossRef](#)]
64. Zhong, Z.H.; Li, C.G.; Zhang, X.Y.; Gu, J.F. The graded microstructures evolving with thermal cycles in pure copper processed by laser metal deposition. *Mater. Lett.* **2018**, *230*, 215–218. [[CrossRef](#)]
65. Sinico, M.; Cogo, G.; Benettoni, M.; Calliari, I.; Pepato, A. Influence of powder particle size distribution on the printability of pure copper for selective laser melting. In Proceedings of the Solid Freeform Symposium 658–667, Austin, TX, USA, 12–14 August 2019.
66. Lingqin, X.; Guang, C.; Luyu, Z.; Pan, L. Explore the feasibility of fabricating pure copper parts with low-laser energy by selective laser melting. *Mater. Res. Expr.* **2020**, *7*, 106509. [[CrossRef](#)]
67. Bonesso, M.; Rebesan, P.; Gennari, C.; Mancin, S.; Dima, R.; Pepato, A.; Calliari, I. Effect of particle size distribution on laser powder bed fusion manufacturability of copper. *Berg. Huetttenmaenn. Monatsh.* **2021**, *166*, 256–262. [[CrossRef](#)]
68. Yang, P.; Guo, X.; He, D.; Tan, Z.; Shao, W.; Fu, H. Selective laser melting of high relative density and high strength parts made of minor surface oxidation treated pure copper powder. *Metals* **2021**, *11*, 1883. [[CrossRef](#)]
69. Jadhav, S.D.; Vleugels, J.; Kruth, J.-P.; van Humbeeck, J.; Vanmeensel, K. Mechanical and electrical properties of selective laser-melted parts produced from surface-oxidized copper powder. *Mater. Des. Proc. Comm.* **2019**, *2*, e94. [[CrossRef](#)]
70. Lindström, V.; Liashenko, O.; Zwiackner, K.; Derevianko, S.; Morozovych, V.; Lyashenko, J.; Leinenbach, C. Laser powder bed fusion of metal coated copper powders. *Materials* **2020**, *13*, 3493. [[CrossRef](#)]
71. Jadhav, S.D.; Dadbakhsh, S.; Vleugels, J.; Hofkens, J.; van Puyvelde, P.; Yang, S.; Kruth, J.-P.; van Humbeeck, J.; Vanmeensel, K. Influence of carbon nanoparticle addition (and impurities) on selective laser melting of pure copper. *Materials* **2019**, *12*, 2469. [[CrossRef](#)]
72. Prasad, H.S.; Brückner, F.; Volpp, J.; Kaplan, A.F.H. Laser metal deposition of copper on diverse materials using green laser sources. *Int. J. Adv. Manuf. Techn.* **2020**, *107*, 1559–1568. [[CrossRef](#)]
73. Pan, L.; Zhang, C.-L.; Liu, T.; Liu, X.-Y.; Liu, J.-L.; Liu, S.; Wang, W.-H.; Zhang, H.-H. Molten pool structure and temperature flow behavior of green-laser powder bed fusion pure copper. *Mater. Res. Expr.* **2022**, *9*, 016504. [[CrossRef](#)]
74. Gruber, S.; Stepien, L.; Lopez, E.; Brueckner, F.; Leyens, C. Physical and geometrical properties of additively manufactured pure copper samples using a green laser source. *Materials* **2021**, *14*, 3642. [[CrossRef](#)]
75. Higashino, R.; Sato, Y.; Masuno, S.; Shobu, T.; Funada, Y.; Abe, N.; Tsukamoto, M. Development of blue diode laser for additive manufacturing. In Proceedings of the SPIE 11271, Laser 3D Manufacturing VII, 1127114, San Francisco, CA, USA, 25 March 2020. [[CrossRef](#)]
76. Kaden, L.; Matthäus, G.; Ramm, R.; Ullsperger, T.; Seyfarth, B.; Nolte, S. Additive manufacturing of pure copper using ultrashort laser pulses. In Proceedings of the SPIE 10909 Laser 3D manufacturing VI, 109090D, San Francisco, CA, USA, 7 June 2019. [[CrossRef](#)]
77. Momeni, S.; Guschlbauer, R.; Osmanlic, F.; Körner, C. Selective electron beam melting of a copper-chrome powder mixture. *Mater. Lett.* **2018**, *223*, 250–252. [[CrossRef](#)]

78. Uchida, S.; Kimura, T.; Nakamoto, T.; Ozaki, T.; Miki, T.; Takemura, M.; Oka, Y.; Tsubota, R. Microstructures and electrical and mechanical properties of Cu-Cr alloys fabricated by selective laser melting. *Mater. Des.* **2019**, *175*, 107815. [[CrossRef](#)]
79. Chen, Y.; Ren, S.; Zhao, Y.; Qu, X. Microstructure and properties of CuCr alloy manufactured by selective laser melting. *J. All. Comp.* **2019**, *786*, 189–197. [[CrossRef](#)]
80. Popovich, A.; Sufiiarov, V.; Polozov, I.; Borisov, E.; Masaylo, D.; Orlov, A. Microstructure and mechanical properties of additive manufactured copper alloy. *Mater. Lett.* **2016**, *179*, 38–41. [[CrossRef](#)]
81. Guan, P.; Chen, X.; Liu, P.; Sun, F.; Zhu, C.; Zhou, H.; Fu, S.; Wu, Z.; Zhu, Y. Effect of selective laser melting process parameters and aging heat treatment on properties of CuCrZr alloy. *Mater. Res. Expr.* **2019**, *6*, 1165c1. [[CrossRef](#)]
82. Artzt, K.; Siggel, M.; Kleinert, J.; Riccius, J.; Requena, G.; Haubrich, J. Pyrometric-based melt pool monitoring study of CuCr1Zr processed using L-PBF. *Materials* **2020**, *13*, 4626. [[CrossRef](#)] [[PubMed](#)]
83. Buchmayr, B.; Panzl, G.; Walzl, A.; Wallis, C. Laser powder bed fusion- Materials issues and optimized processing parameters of tool steels, AlSiMg- and CuCrZr-alloys. *Adv. Eng. Mater.* **2017**, *19*, 1600667. [[CrossRef](#)]
84. Wegener, T.; Koopmann, J.; Richter, J.; Krooß, P.; Niendorf, T. CuCrZr processed by laser powder bed fusion- Processability and influence of heat treatment on electrical conductivity, microstructure and mechanical properties. *Fatigue Fract. Eng. Mater. Struct.* **2021**, *44*, 2570–2590. [[CrossRef](#)]
85. Jahns, K.; Bappert, R.; Böhlke, P.; Krupp, U. Additive manufacturing of CuCrZr1 by development of a gas atomization and laser powder bed fusion routine. *Int. J. Adv. Manuf. Techn.* **2020**, *107*, 2151–2161. [[CrossRef](#)]
86. Ordás, N.; Portolés, L.; Azpeleta, M.; Gómez, A.; Blasco, J.R.; Martinez, M.; Ureña, J.; Iturriza, I. Development of CuCrZr via electron beam powder bed fusion (EB-PBF). *J. Nucl. Mater.* **2021**, *548*, 152841. [[CrossRef](#)]
87. Maischner, D.; Fritsching, U.; Kini, A.; Weisheit, A.; Uhlenwinkel, V.; Schleifenbaum, J.H.; Biermann, T. Laser additive manufacturing of copper-chromium-niobium alloys using gas atomized powder. *Int. J. Mater. Res.* **2020**, *111*, 587–593. [[CrossRef](#)]
88. Kini, A.R.; Maischner, D.; Weisheit, A.; Ponge, D.; Gault, B.; Jägle, E.A.; Raabe, D. In-situ synthesis via laser metal deposition of a lean Cu-3.4Cr-0.6Nb (at.%) conductive alloy hardened by Cr nano-scale precipitates and by laves phase micro-particles. *Acta Mater.* **2020**, *197*, 330–340. [[CrossRef](#)]
89. Landes, S. Characterization of directed energy deposition additively manufactured GRCop-42 alloy. In *Electronic Theses and Dissertations*; South Dakota State University: Brookings, SD, USA, 2020; p. 5036. Available online: <https://openprairie.sdstate.edu/etd/5036> (accessed on 7 September 2022).
90. Seltzman, A.H.; Wukitch, S.J. RF losses in selective laser melted GRCop-84 copper waveguide for an additively manufactured lower hybrid current drive launcher. *Fus. Eng. Des.* **2020**, *159*, 111762. [[CrossRef](#)]
91. Seltzman, A.H.; Wukitch, S.J. Precipitate size in GRCop-84 gas atomized powder and laser powder bed fusion additively manufactured material. *Fus. Sci. Techn.* **2021**, *77*, 641–646. [[CrossRef](#)]
92. Seltzman, A.H.; Wukitch, S.J. Nuclear response of additively manufactured GRCop-84 copper for use in lower hybrid launchers in a fusion environment. *Fus. Eng. Des.* **2020**, *159*, 111726. [[CrossRef](#)]
93. Seltzman, A.H.; Wukitch, S.J. Resolution and geometric limitations in laser powder bed fusion additively manufactured GRCop-84 structures for a lower hybrid current drive launcher. *Fus. Eng. Des.* **2021**, *173*, 112847. [[CrossRef](#)]
94. Hayes, C.; Brown, E.; Kappes, B. Characterization of selective laser melted GRCop-84. In *Proceedings of the Joint Propulsion Conference*, Cincinnati, OH, USA, 9–11 July 2018. [[CrossRef](#)]
95. Demeneghi, G.; Barnes, B.; Gradl, P.; Mayeur, J.R.; Hazeli, K. Size effects on microstructure and mechanical properties of additively manufactured copper-chromium-niobium alloy. *Mater. Sci. Eng. A* **2021**, *820*, 141511. [[CrossRef](#)]
96. Ren, Y.; Liu, Z.; Zhang, Y.; Al, Y.; Ye, S.; Li, J.; Peng, W. Optimization of process parameters for selective laser melting of Cu-Cr-Nb alloy. *Mater. Sci. Eng. Powder Met.* **2022**, *27*, 66–76. [[CrossRef](#)]
97. Doñate-Buendia, C.; Frömel, F.; Wilms, M.B.; Streubel, R.; Tenkamp, J.; Hupfeld, T.; Nachev, M.; Gökce, E.; Weisheit, A.; Barcikowski, S.; et al. Oxide dispersion-strengthened alloys generated by laser metal deposition of laser-generated nanoparticle-metal powder composites. *Mater. Des.* **2018**, *154*, 360–369. [[CrossRef](#)]
98. Zhou, D.; Geng, H.; Zeng, W.; Zheng, D.; Pan, H.; Kong, C.; Munroe, P.; Sha, G.; Suryanarayana, C.; Zhang, D. High temperature stabilization of a nanostructured Cu-Y₂O₃ composite through microalloying with Ti. *Mater. Sci. Eng. A* **2018**, *712*, 80–87. [[CrossRef](#)]
99. Zhou, J.; Yi, G.; Zhang, P.; Yin, S.; Xue, L.; Yan, Y. The microstructure, mechanical-thermal properties and softening resistance of Y4Al2O9 dispersion-strengthened Cu alloy. *J. Nucl. Mater.* **2022**, *560*, 153484. [[CrossRef](#)]
100. Groza, J.R.; Gibeling, J.C. Principles of particle selection for dispersion-strengthened copper. *Mater. Sci. Eng. A* **1993**, *171*, 115–125. [[CrossRef](#)]
101. Uchida, Y.; Ohnuki, S.; Hashimoto, N.; Suda, T.; Nagai, T.; Shibayama, T.; Hamada, K.; Akasaka, N.; Yamashita, S.; Ohstuka, S.; et al. Effect of minor alloying element on dispersing nano-particles in ODS steel. *MRS Online Proc. Libr.* **2006**, *981*, 709. [[CrossRef](#)]
102. Caiazza, F.; Alfieri, V.; Casalino, G. On the relevance of volumetric energy density in the investigation of Inconel 718 laser powder bed fusion. *Materials* **2020**, *13*, 538. [[CrossRef](#)]
103. Slotwinski, J.A.; Garboczi, E.J.; Stuzman, P.E.; Ferraris, C.F.; Watson, S.S.; Peltz, M.A. Characterization of metal powders used for additive manufacturing. *J. Res. Nat. Inst. Stand. Techn.* **2014**, *119*, 460–493. [[CrossRef](#)]
104. Urionabarrenetxea, E.; Avello, A.; Rivas, A.; Martin, J.M. Experimental study of the influence of operational and geometric variables on the powders produced by close-coupled gas atomisation. *Mater. Des.* **2021**, *199*, 109441. [[CrossRef](#)]

105. Li, D.; Robinson, M.B.; Rathz, T.J.; Williams, G. Liquidus temperatures and solidification behavior in the copper-niobium system. *Acta Mater.* **1998**, *46*, 3849–3855. [[CrossRef](#)]
106. Bor, A.; Jargalsaikhan, B.; Uranchimeg, K.; Lee, J.; Choi, H. Particle morphology control of metal powder with various experimental conditions using ball milling. *Powder Techn.* **2021**, *394*, 181–190. [[CrossRef](#)]
107. Vasquez, E.; Giroux, P.-F.; Lomello, F.; Nussbaum, M.; Maskrot, H.; Schuster, F.; Castagny, P. Effect of powder characteristics on production of oxide dispersion strengthened Fe-14Cr steel by laser powder bed fusion. *Powder Techn.* **2020**, *360*, 998–1005. [[CrossRef](#)]
108. Suryanarayana, C. Mechanical alloying and milling. *Progr. Mater. Sci.* **2001**, *46*, 1–184. [[CrossRef](#)]
109. Tertuliano, O.A.; DePond, P.J.; Doan, D.; Matthews, M.J.; Gu, X.W.; Cai, W. Nanoparticle-enhanced absorptivity of copper during laser powder bed fusion. *Addit. Manuf.* **2022**, *51*, 102562. [[CrossRef](#)]
110. Kruth, J.P.; Wang, X.; Laoui, T.; Froyen, L. Lasers and materials in selective laser sintering. *Assem. Autom.* **2003**, *23*, 357–371. [[CrossRef](#)]
111. Ren, Z.; Zhang, D.Z.; Fu, G.; Jiang, J.; Zhao, M. High-fidelity modelling of selective laser melting copper alloy: Laser reflection behaviour and thermal fluid dynamics. *Mater. Des.* **2021**, *207*, 109857. [[CrossRef](#)]
112. Yang, Y.H.; Lei, Q.; Zhang, P.; Wang, W.Y.; Zhang, X.K.; Li, Y.P.; Zhou, K.C.; Li, Z. Stabilization of L12 structured Cr3Cu precipitates in a Cu-4.06Cr-1.25Nb alloy with high temperature strength. *Mater. Res. Lett.* **2022**, *10*, 257–263. [[CrossRef](#)]
113. Yang, Y.; Lei, Q.; Liu, H.; Hong, J.; Han, Z.; An, Q.; Shan, J.; Chen, X.; Xu, H.; Xiao, Z.; et al. Cr-based second phases in a high conductivity Cu-Cr-Nb alloy with high high-temperature strength. *Mater. Des.* **2022**, *219*, 110784. [[CrossRef](#)]
114. Fu, J.; Davis, T.P.; Kumar, A.; Richardson, I.M.; Hermans, M.J.M. Characterisation of the influence of vanadium and tantalum on yttrium-based nano-oxides in ODS Eurofer steel. *Mater. Charact.* **2021**, *175*, 111072. [[CrossRef](#)]
115. Xu, H.; Lu, Z.; Wang, D.; Liu, C. Microstructure refinement and strengthening mechanisms of a 9Cr oxide dispersion strengthened steel by zirconium addition. *Nucl. Eng. Techn.* **2017**, *49*, 178–188. [[CrossRef](#)]
116. Park, J.J.; Hong, S.M.; Park, E.K.; Lee, M.K.; Rhee, C.K. Synthesis of Fe based ODS alloys by a very high speed planetary milling process. *J. Nucl. Mater.* **2012**, *428*, 35–39. [[CrossRef](#)]
117. Tan, L.; Wang, G.; Guo, Y.; Fang, Q.; Liu, Z.; Xiao, X.; He, W.; Qin, Z.; Zhang, Y.; Liu, F.; et al. Additively manufactured oxide dispersion strengthened nickel-based superalloy with superior high temperature properties. *Virt. Phys. Prototyp.* **2020**, *15*, 555–569. [[CrossRef](#)]
118. Chinnappan, R. Thermodynamic stability of oxide phases of Fe-Cr based ODS steels via quantum mechanical calculations. *Proc. Eng.* **2014**, *86*, 788–798. [[CrossRef](#)]
119. Rittinghaus, S.-K.; Wilms, M.B. Oxide dispersion strengthening of γ -TiAl laser additive manufacturing. *J. All. Comp.* **2019**, *804*, 457–460. [[CrossRef](#)]
120. Anderson, K.R.; Groza, J.R. Microstructural size effects in high-strength high-conductivity Cu-Cr-Nb alloys. *Met. Mater. Trans A* **2001**, *32*, 1211–1224. [[CrossRef](#)]
121. Kürnsteiner, P.; Wilms, M.B.; Weisheit, A.; Barriobero-Vila, P.; Jäggle, E.A.; Raabe, D. Massive nanoprecipitation in a Fe-19Ni-xAl maraging steel triggered by the intrinsic heat treatment during laser metal deposition. *Acta Mater.* **2017**, *129*, 52–60. [[CrossRef](#)]
122. Kürnsteiner, P.; Wilms, M.B.; Weisheit, A.; Gault, B.; Jäggle, E.A.; Raabe, D. High-strength Damascus steel by additive manufacturing. *Nature* **2020**, *582*, 515–519. [[CrossRef](#)]
123. Kürnsteiner, P.; Bajaj, P.; Gupta, A.; Wilms, M.B.; Weisheit, A.; Li, X.; Leinenbach, C.; Gault, B.; Jäggle, E.A.; Raabe, D. Control of thermally stable core-shell nano-precipitates in additively manufactured Al-Sc-Zr alloys. *Addit. Manuf.* **2020**, *32*, 100910. [[CrossRef](#)]
124. Rittinghaus, S.-K.; Amr, A.; Hecht, U. Intrinsic heat treatment of an additively manufactured medium entropy AlCrFe₂Ni₂-alloy. *Met. Mater. Int.* **2022**, 1–12. [[CrossRef](#)]